



Noble-metal-free heterostructure for efficient hydrogen evolution in visible region: Molybdenum nitride/ultrathin graphitic carbon nitride

Shuaiqi Gong^a, ZhengJun Jiang^a, Penghui Shi^{a,b,*}, Jinchen Fan^{a,b}, Qunjie Xu^{a,b,*}, Yulin Min^{a,b,*}

^a Shanghai Key Laboratory of Materials Protection and Advanced Materials in Electric Power, Shanghai University of Electric Power, Shanghai 200090, PR China

^b Shanghai Institute of Pollution Control and Ecological Security, Shanghai 200092, PR China

ARTICLE INFO

Keywords:

Mo₂N
Ultrathin g-C₃N₄ nanosheet
Hydrogen evolution
Visible-light photocatalysis

ABSTRACT

Molybdenum nitride (MoN) has been attracting increasing attention in recent years for the application of electrocatalytic hydrogen evolution reaction. However, the application of MoN for photocatalytic H₂ evolution has seldom been reported. Here, we report that the sample with the heterostructure between Mo₂N and 2D ultrathin g-C₃N₄ nanosheet (CN) is fabricated via boil bathing method for the use of the visible light photocatalytic H₂ evolution. Without using any noble metal cocatalyst, the H₂ evolution rate of Mo₂N/CN under visible light irradiation reaches 0.89 μmol g⁻¹ h⁻¹, which is ≈ 148 times higher than that of pure CN. The photoelectron-chemical experiments suggest that the carriers in Mo₂N/CN can separate and transfer easier than those in CN due to the effect of Mo₂N as the modification of CN. The combination of the Mo₂N and CN represents not only a simple but also an economical and powerful method for the highly effective photocatalytic H₂ generation in the visible region.

1. Introduction

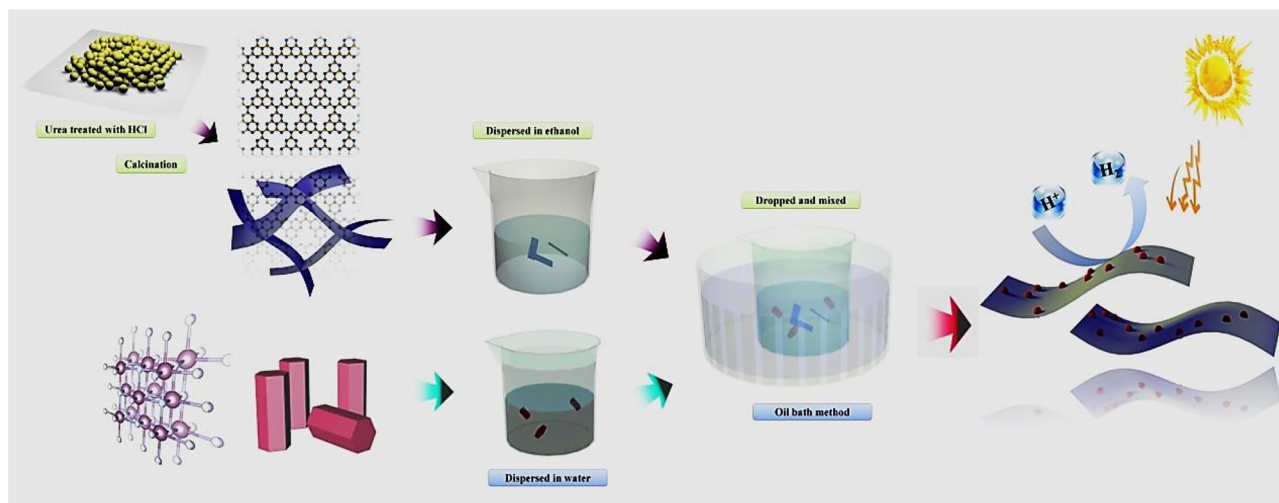
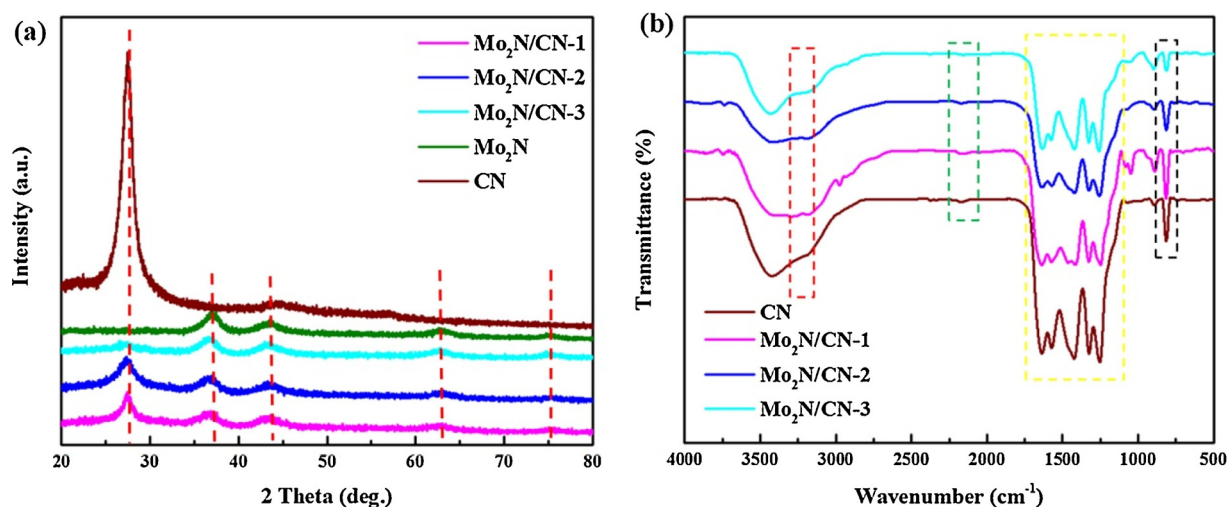
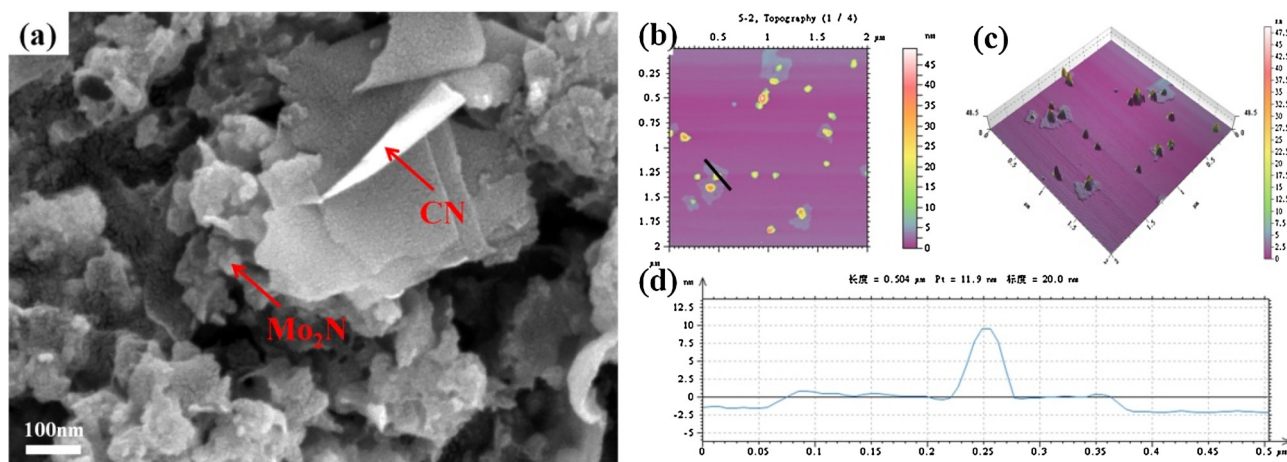
Concentrating on the energy crisis and the increasing environmental issues which are caused by the excessive consumption of fossil fuels, renewable and clean energy sources are intensively demanded in modern society [1]. Hydrogen (H₂) is undeniably pursued as one of the most promising candidates for green energy carries to solve the energy problems because of its zero carbon footprints and high mass-specific energy density [2,3]. Among all kinds of hydrogen evolution processes, splitting water using solar energy is believed to be the most sustainable option. In the past decades, researchers always aim to find high performance and low-cost photocatalysts toward water splitting. At present, the energy conversion efficiency of solar-to-hydrogen is still too low although H₂ can be obtained directly using semiconductor photocatalysts under light irradiation. The main barriers are the lack of suitable photocatalysts which can meet the following requirements: (1) absorbing broadband light; (2) efficient separation and fast transfer of photogenerated electron-hole pairs [4]. To address these requirements, many great efforts have been made by using diversified semiconductor photocatalysts or doping noble metals such as Pt as cocatalysts to promote charge separation. However, the terrestrial scarcity and high cost of noble metals limit the viability of H₂ production and commercial applications. So, these obstacles have been motivated to design and develop non-noble metal cocatalysts with photocatalysts to

promote the efficient charge separation from the semiconductor to the surface on the cocatalyst, from which H₂ is obtained by reducing H₂O [5,6].

Currently, a wealth of materials responding to the visible-light spectrum which occupies around 46% of the solar light are designed as photocatalysts to achieve effective solar hydrogen production from water, such as sulfide [7], nitride [8], vanadates [9], phosphides [10], and metal oxides [11]. However, their commercial applications are hindered due to the high cost, risks for the environment or inadequate scalability [12]. Polymeric graphitic carbon nitride (g-C₃N₄) has recently shown promise for driving photocatalytic H₂ production owing to its chemical stability and amazing electronic structure [13–16]. The bulk g-C₃N₄ is usually synthesized by thermal polymerization of melamine, urea, or dicyanamide. It possesses a large bandgap at about 2.7 eV, and its highest occupied molecular orbital (HOMO) and lowest unoccupied molecular orbital (LUMO) situated at +1.6 V and -1.1 V versus normal hydrogen electrode, respectively. Although it is cheap and non-toxic, the pristine g-C₃N₄ is still limited by the poor visible light absorption (λ < 460 nm), fast recombination of photoinduced electron-hole pairs, low surface area, and limited active sites [15,17]. In order to challenge these limitations, various strategies have been made to improve the photocatalytic properties of g-C₃N₄, such as synthesizing specific nanostructures of g-C₃N₄ [18,19], doping with metal (e.g. Pt) or non-metal, (e.g. C [20], S [21]), building heterostructure between g-

* Corresponding authors at: College of Environmental and Chemical Engineering, Shanghai University of Electric Power, 200090, PR China.

E-mail addresses: shipenghui@shiep.edu.cn (P. Shi), xuqunjie@shiep.edu.cn (Q. Xu), ahaqmylin@126.com (Y. Min).

Scheme 1. The process of synthesizing Mo₂N/CN.Fig. 1. XRD patterns of CN, Mo₂N, and Mo₂N/CN-x (a), and FTIR patterns of CN and Mo₂N/CN-x (b).Fig. 2. SEM image of Mo₂N/CN (a). AFM (b, c, d) images of Mo₂N/CN and the corresponding height profile of the black line part in (b).

C₃N₄ and other semiconductors. For instance, Xiong's group [22] builds metal-to-ligand charge transfer between Pt²⁺ and g-C₃N₄, achieving broad light-absorption at the visible-near-infrared area and high H₂ production rate.

However, high cost and scarcity of Pt have limited practical

applications. It has been proved that loading cocatalysts can not only speed up electron transport but also act as electron sinks to provide further charge separation across the interface [23]. Many non-noble metal cocatalysts have received much attention such as two-dimensional (2D) molybdenum disulfide (MoS₂) owing to its high mobility for

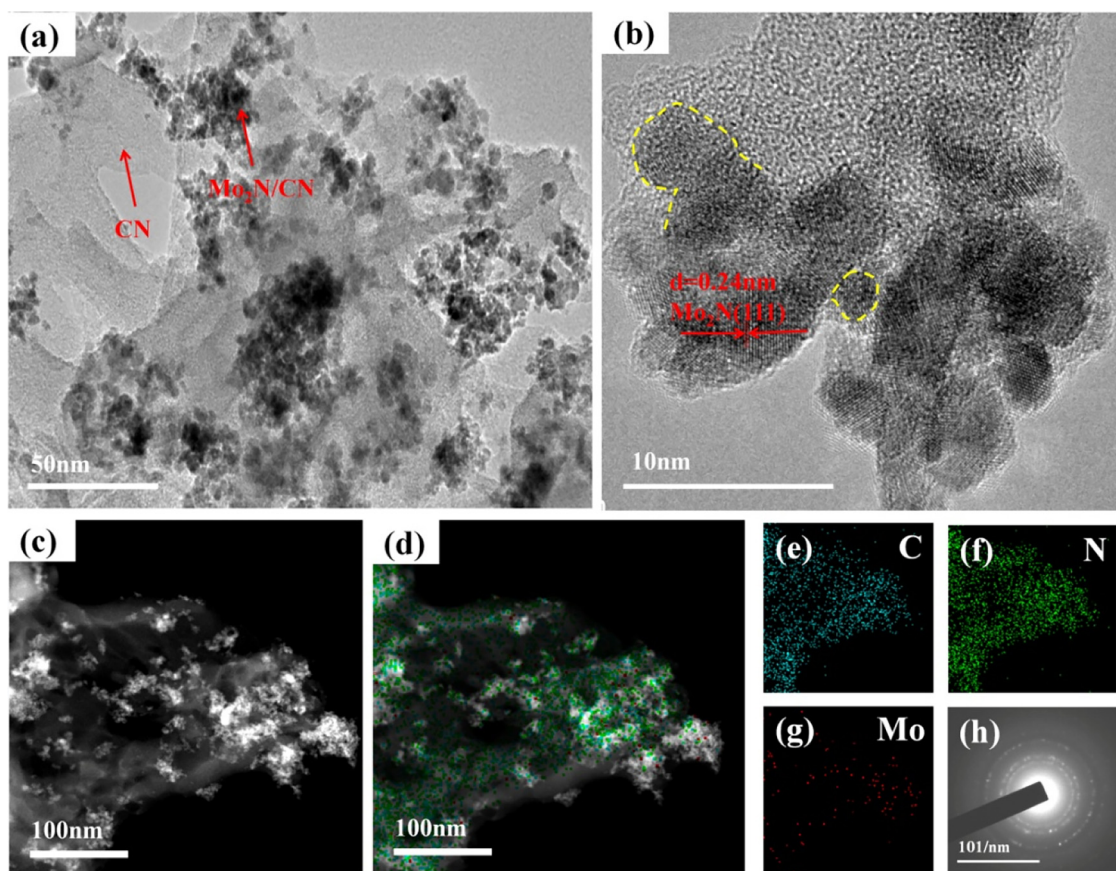


Fig. 3. TEM (a), HETEM (b), STEM (c), EDX elemental mapping of all elements (d), and C (e), N (f), Mo (g) element, and Electron diffraction (g) images of Mo₂N/CN.

charge transport [24,25]. To date, transition metal sulfides [26], nitrides [27], carbides [28], and oxides [30] have accumulated hot research in H₂ production, especially Molybdenum (Mo)-based catalysts. Notable recent progress has been made in developing Mo-based photocatalysts resulting in the excellent electrocatalytic H₂ evolution. For instance, Zong et al. [29] deposits MoS₂ on the surface of CdS, and the H₂ evolution rate can increase up to 36 times than that of pure CdS with only 0.2 wt% of MoS₂. Mai group [30] have reported a MoB/g-C₃N₄ Schottky catalyst which had a remarkable H₂ production activity. Typically, Mo-based catalysts are emerging as promising alternatives for noble metal catalysts in H₂ production from water splitting. They can exhibit moderate H₂ binding energy on catalytic centers like Pt and excellent transport property in solid like metallic. Transition-metal nitrides have attracted much attention in electrocatalysis applications, as they show high conductivity, low electrical resistance, superior corrosion stability, and excellent mechanical strength [31,32]. It has previously been reported that MoN showed high H₂ evolution rate as an electrocatalyst [33,34]. It is well known that MoN possesses hexagonal crystal structure with a layer configuration. Cui et al. [34] have synthesized MoN layers which are comprised of apical Mo atoms, which can confirm that the surface Mo atoms play roles as the active sites for transforming protons into hydrogen. Furthermore, the 2D structure is beneficial for the exposure of abundant surface active sites and reducing the charge migration distance [35]. Here, it is interesting that the above-mentioned intriguing effects and properties can be manifested in a new photocatalyst heterostructure comprised of Mo₂N and g-C₃N₄ for highly efficient H₂ production. As we know, the 2D ultrathin structure has been developed due to the large exposed active sites on the surface and/or edge of the nanosheets [36]. Mo₂N nanoparticles can be loaded on the 2D ultrathin g-C₃N₄ nanosheets (CN). The Mo₂N nanoparticles obtained through oil bath method from bulk Mo₂N can disperse on the surface of CN evenly, causing the full combination between Mo₂N and

CN. As well, we gained CN by the method of acid-assisted calcination. The heterojunction formed at the metal-semiconductor interface is integrated through the boil bath treatment of Mo₂N nanoparticles and CN. Our concept is to take advantage of the strong interfacial interaction when Mo₂N nanoparticles can be supported on junction-matched CN as cocatalysts and efficient charge transfer at the interface to enhance the charge separation and transportation for the operation of CN so that it can impede the fast recombination of CN. As a result, compared with bulk CN, the Mo₂N/CN can exhibit higher H₂ generation rate (0.89 $\mu\text{mol g}^{-1} \text{h}^{-1}$), which is 143 times than CN, and the light absorption edge had a red-shift. Accordingly, this type of photocatalyst heterostructure can accelerate the transfer of charges and block the recombination of carriers, contributing to a new plan for designing g-C₃N₄-based photocatalysts in renewable clean energy conversion.

2. Experimental

2.1. Chemical and reagents

Urea (CH₄N₂O, AR, 99%), Ammonium molybdate tetrahydrate, ((NH₄)₄Mo₇O₂₄·4H₂O, AR), Ethyl Cellulose ([C₆+2nH₇+8nO₂+4n]_x, CP), and α -Terpineol (C₁₀H₁₈O, 98%) are purchased from Shanghai Aladdin Reagent Co., Ltd., China. Triethylamine (TEOA, 99.0–110.0%, AR) is obtained from GENERAL-REAGENT. Hexamethylenetetramine (HMT) is purchased from Shanghai Junhui Chemical Co., Ltd. All reagents are used without further purification.

2.2. Preparation of bulk Mo₂N

Bulk Mo₂N was fabricated via annealing Mo-containing precursor under an ammonia atmosphere. In detail, 3 g (NH₄)₄Mo₇O₂₄·4H₂O was added to the 50 mL double distilled water with stirring under 40°C

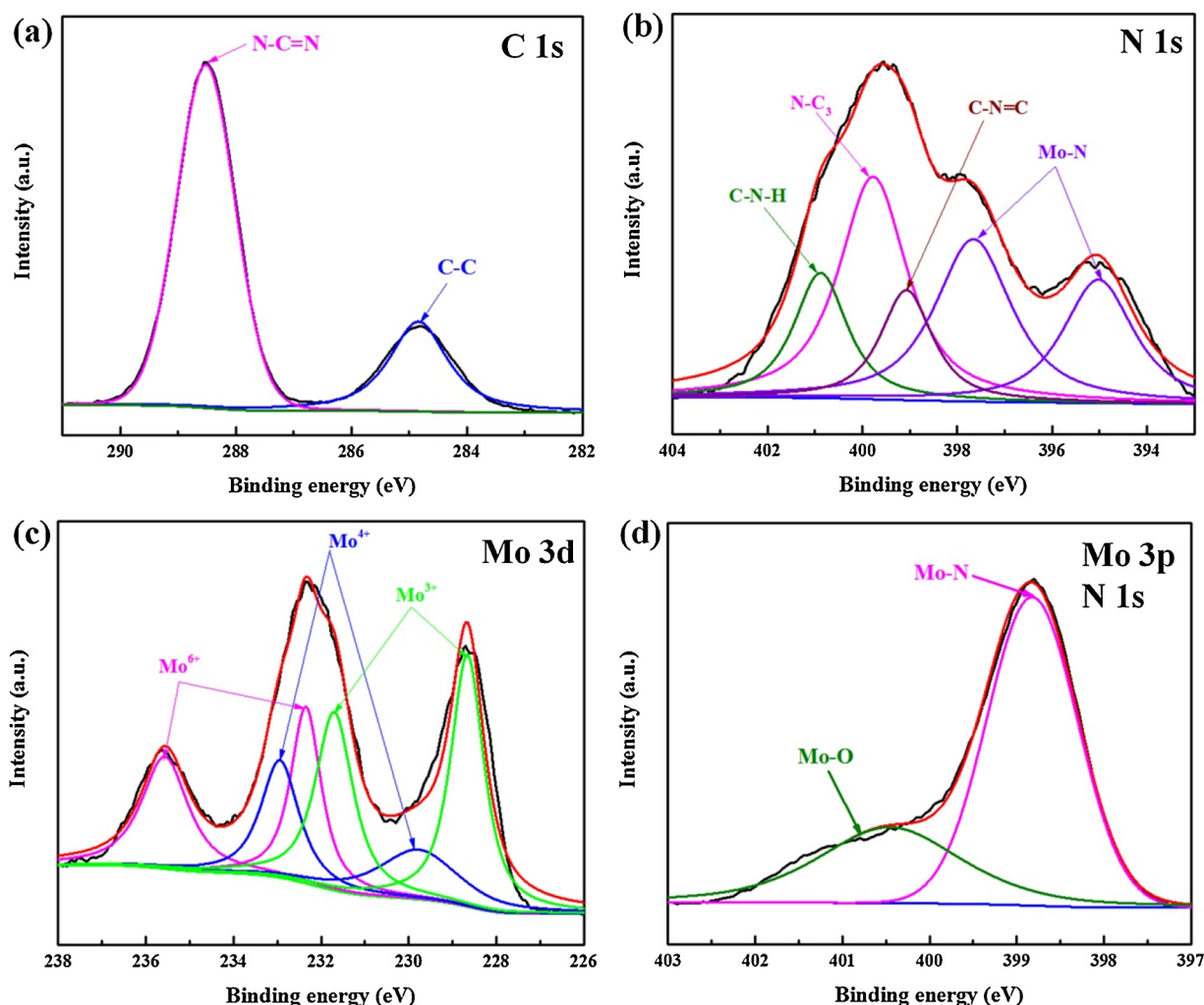


Fig. 4. XPS spectra of C 1s (a), N 1s (b), Mo 3d (c) and Mo 3p-N 1s (d) of MoN/g-C₃N₄.

water bathing to obtain a clarified solution. Then, it was dropped into 50 mL hexamethylenetetramine (HMT) solution with 6 g HMT. And the mixture was stirred for 6 h. The solid precursor was collected by centrifuging with water and drying at 70°C. The precursor was then annealed at 600°C for 6 h under ammonia flow with a heating rate of 5°C/min. Finally, the dark MoN bulk was obtained.

2.3. Preparation of ultrathin g-C₃N₄ nanosheets

The ultrathin g-C₃N₄ nanosheets (CN) were synthesized by a thermal polymerization method. Typically, 10 g of urea was dissolved in 15 mL double distilled water. Then, adjust the pH of the solution to 4–5 by dropping 0.1 M HCl under stirring. After that, the solution was moved into the 60°C atmosphere to dry.

The urea powders after treating with HCl were heated to 520°C in a tube furnace for 4 h under an N₂ atmosphere at a heating rate of 5°C/min and cooled to room temperature naturally.

2.4. Preparation of Mo₂N/CN-1

Mo₂N/CN-1 were prepared by oil bath method. Typically, 50 mg bulk Mo₂N powders were dispersed in 30 mL double distilled water with ultrasonic for 10 min. Then, transfer into oil bath under 60 °C with stirring. Add 50 mg CN to 30 mL anhydrous ethanol. After ultrasound for an hour to gain the equal dispersions, drop the CN/ethanol dispersion into the Mo₂N/water dispersion. The stirring lasted for 8 h in

the 60 °C boil bath. Finally, Mo₂N/CN-1 was obtained by drying overnight after centrifugation at 8000 rpm for 10 min and washing with ethanol and water.

The preparation of Mo₂N/CN-2 is the same as Mo₂N/CN-1, except the amount of Mo₂N and CN was 50 mg and 100 mg, respectively. And the amount of Mo₂N and CN in Mo₂N/CN-3 was 100 mg and 50 mg accordingly.

2.5. Characterization

The X-ray diffraction (XRD) characterization was carried on a Bruker-AXS D8 Advance in the angular range of 10° to 80° in 2θ angle. The Fourier transform infrared (FTIR) spectra were measured in KBr pellets by Shimadzu 8400S. X-ray photoelectron spectroscopy (XPS) was conducted on a Kratos Axis UltraDLD with Al Kα X-ray (1486.6 eV) radiation. The measurement of scanning electron microscopy (SEM) images were obtained on a field emission scanning electron microscope (FESEM, JEOL, FEG-XL30S). Transmission electron microscopy (TEM) images were collected on JEOL JEM-2100 F with Cs correction. The atomic force microscopy (AFM) images were performed on Agilent 5500AFM with the sample powders dispersing into ethanol. The UV–vis diffuse reflectance spectra (UV–vis-DRS) were carried by using a spectrophotometer (Shimadzu, UV-2401PC), and BaSO₄ was used as the reference. The Photoluminescence (PL) images were measured on RF-5301 PC with an excitation wavelength of 416 nm. The H₂ detection was collected by gas chromatography (Techcomp, GC7900). All the

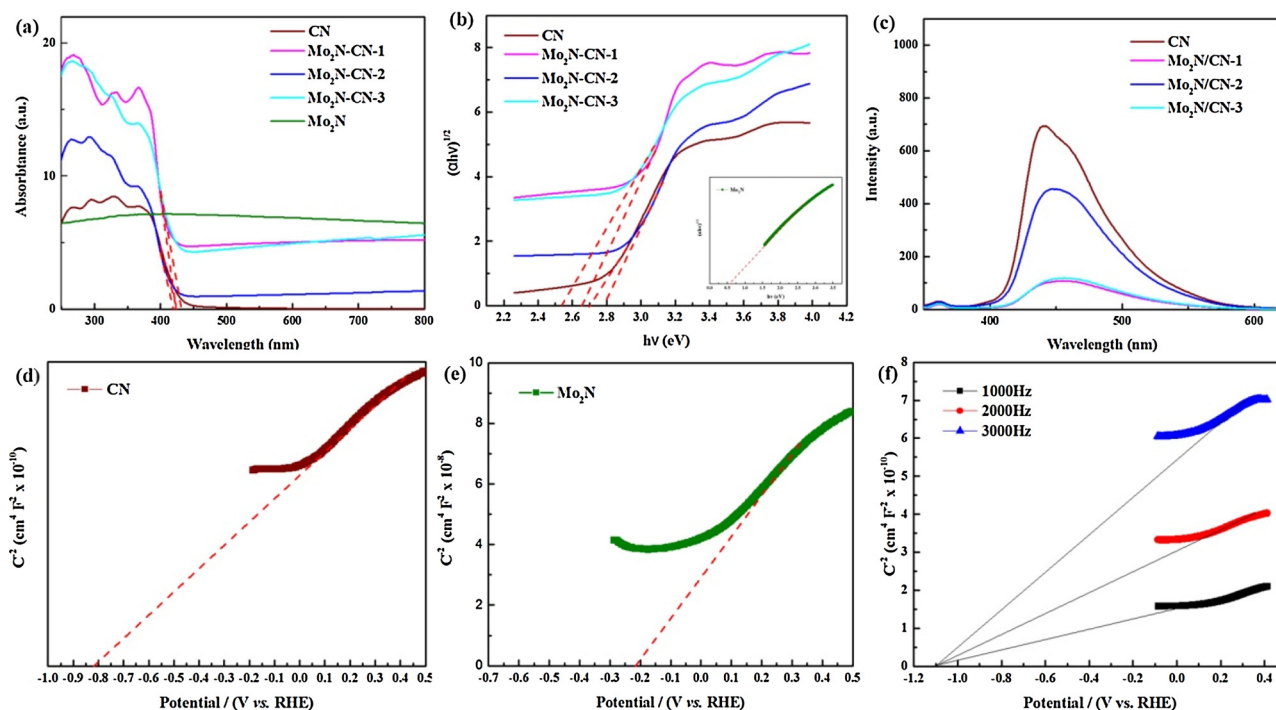


Fig. 5. UV-vis diffuse reflectance (a). Plots of transformed Kubelka-Munk functions of CN, Mo₂N/CN-x (b), and Mo₂N (insert of b). The PL spectra of CN and Mo₂N/CN-x (c), the Mott-Schottky plots (MS) of CN(d), Mo₂N (e), and Mo₂N/CN-1 (f).

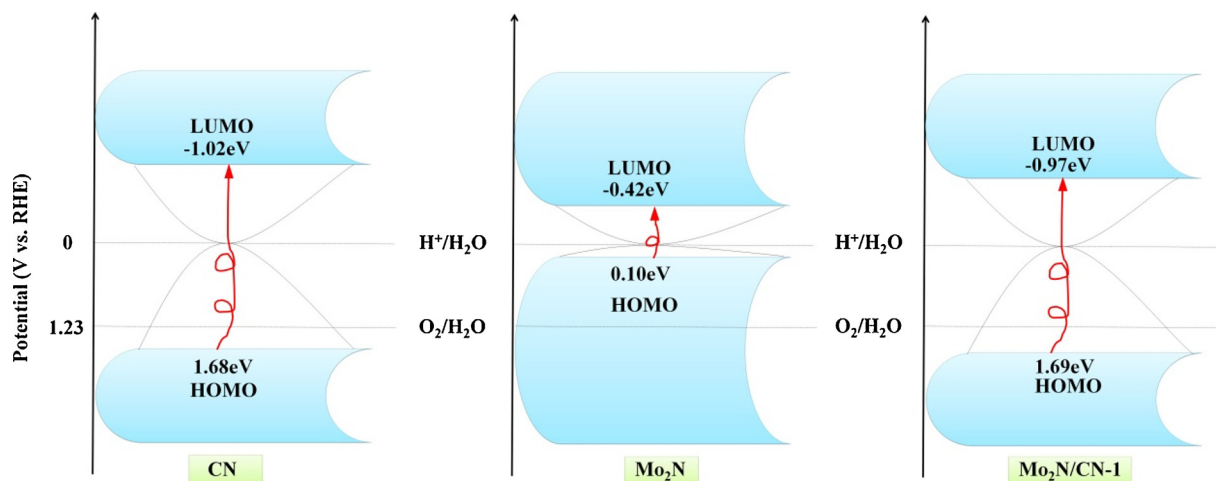


Fig. 6. Band structure alignments for pure CN, Mo₂N and Mo₂N/CN-1.

light irradiations were achieved by using a 300 W xenon light source as simulated sunlight with filters of $\lambda > 420$ nm (PerfectLight, PLS-SXE 300E).

2.6. Photoelectrochemical measurements

CN, and Mo₂N/CN modified FTO electrodes were prepared by following procedures: 7.5 mg samples were added to 1 mL α -Terpineol, then 1 mg Ethyl Cellulose were added. After that add 0.5 mL ethanol to stir for 24 h to form a homogenous suspension. Finally, a certain amount of the above suspension was coated onto the surface of FTO electrode with an area of 1 cm × 1 cm to form a uniform thickness film, then dried at 60 °C in an oven.

Photoelectrochemical measurements were carried out in a standard three-electrode cell system using a CHI660E electrochemistry workstation in ambient atmosphere at room temperature devised of the as-synthesized materials modified FTO, Ag/AgCl electrode, and Pt wire as

working, counter, and reference electrodes, respectively. We measured photocurrent response, electrochemical impedance spectroscopy (EIS), linear sweep voltammetry (LSV) and Mott-Schottky (MS) plots in 0.5 M Na₂SO₄ electrolyte. The photocurrent responses were recorded at an electrode potential of 0.2 V and the interval between light on a light off was 10 s. The LSV curves were obtained with a scan rate of 50 mV s⁻¹. For the photoelectrochemical experiments, the working electrodes were irradiated by a 30 W xenon lamp coupled with a UV cut-off filter ($\lambda > 420$ nm).

2.7. Photocatalytic H₂ evolution

5 mg samples were dispersed in 10 mL of a TEOA-H₂O solution (V_{TEOA} : V_{H₂O} = 1 : 4). And treat the suspension by an ultrasonic bath for 10 min. Then the system was deaerated by N₂ bubbling into the dispersion for 2 h to completely remove the dissolved oxygen. Afterward, the system was irradiated by using a xenon lamp with a

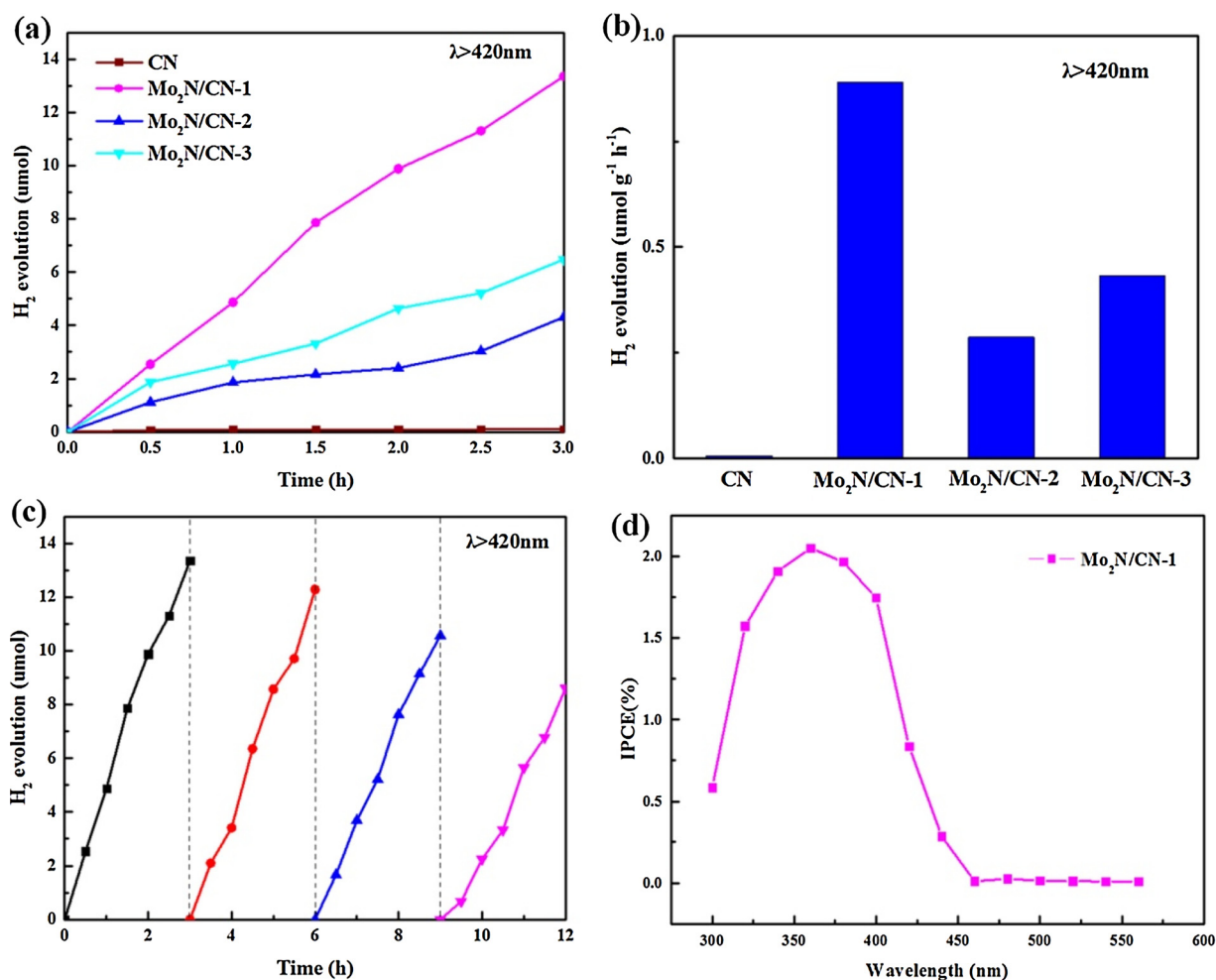


Fig. 7. Photocatalytic H₂ generation from water containing TEOA (20 vol%) on different catalysts under visible light ($\lambda > 420$ nm) irradiation: amount of H₂ generation (a) and H₂ generation rate (b) of CN, Mo₂N/CN-1, Mo₂N/CN-2, and Mo₂N/CN-3. Cycling stability test on Mo₂N/CN-1 (c). Monochromatic incident photon-to-electron conversion efficiency (IPCE) of Mo₂N/CN-1 (d).

420 nm cutoff filter and stirred continuously. The light intensity was 15 A. The volume of the produced H₂ was analyzed with a gas chromatograph (Techcomp, GC7900). For recycle experiments, the catalysts were collected by high-speed centrifugation after the last round of photoreaction and did the same steps as what the first recycle did.

3. Result and discussion

The Mo₂N/CN heterostructures were fabricated by oil bath method as shown in Scheme 1. Initially, the Mo₂N nanoparticles were synthesized during the process of formatting Mo₂N/CN heterostructures via oil bath. Also, the CN was obtained via the thermal polymerization of urea which was handled by HCl. Finally, the perfect Mo₂N/CN heterostructures were achieved after oil bath under 70°C.

XRD patterns (Fig. 1a) showed that all the diffraction peaks of Mo₂N and CN are well displayed in Mo₂N/CN without any impurity peak. Mo₂N belongs to the space group of Pm3m (221), and the diffraction peaks corresponding to 37.4°, 43.5°, 63.1° and 75.7° are indexed as (111), (200), (220), and (311) diffraction planes respectively. For CN, the clear peak at 27.3° indexing as (002) was detected. [13,37,38] For Mo₂N/CN, typical diffraction peaks of both Mo₂N and CN can be all observed. However, the represented peak of CN at 27.3° shows a lower intensity in Mo₂N/CN standing its crystallinity was reduced. Also, there is a little blue shift for the peaks of Mo₂N/CN than the pure materials. Totally, Mo₂N and CN have been composited successfully according to the Mo₂N/CN patterns.

The Mo₂N/CN samples have been further characterized using FTIR. As shown in Fig. 1b, the FTIR spectrum for Mo₂N/CN shows nearly similar peaks with CN, from which a peak at 812 cm⁻¹ can be identified for the out-of-plane bending mode of tri-s-triazine rings. Peaks locked between 1000 and 1800 cm⁻¹ can correspond to N–C=N heterorings. In detail, the absorption bands at 1247, 1319 and 1437 cm⁻¹ displayed C–N stretching vibration modes, and the peaks at 1562 and 1643 cm⁻¹ can be connected to the C–N heterocycle stretching vibration modes. Also, a weak peak at around 2158 cm⁻¹ will be belonging to an asymmetric stretching vibration of cyano groups (–C≡N). In addition, multiple broad peaks in the area of 3000–3500 cm⁻¹ exhibit the obvious N–H stretching vibrations.

To investigate the morphology and structure of Mo₂N/CN, SEM, TEM and AFM images are investigated. (Figs. 2 and 3) The SEM images in Fig. 2a have revealed Mo₂N nanoparticles can be dispersed on the nanosheet-layer shape of CN. And the TEM image as shown in Fig. 3a further confirms that the Mo₂N nanoparticles have been attached to the surface of the thin CN nanosheet, which can also be observed in AFM images (Fig. 1b and c), testing the successful combination of Mo₂N and CN after oil bath treatment. As seen from the SEM image in Fig. S1, the CN samples can also be confirmed the 2D sheet-like structure with ultrathin morphology. Meanwhile, a uniform thickness of around 2 nm of the CN is shown in Fig. S1c and S1d, suggesting that the CN comprises about 5 layers (the theoretical thickness of a monolayer of g-C₃N₄ is about 0.4 nm) [39,40]. The unique ultrathin nanosheet morphology of CN can avoid the disadvantage of bulk g-C₃N₄ which hinder light

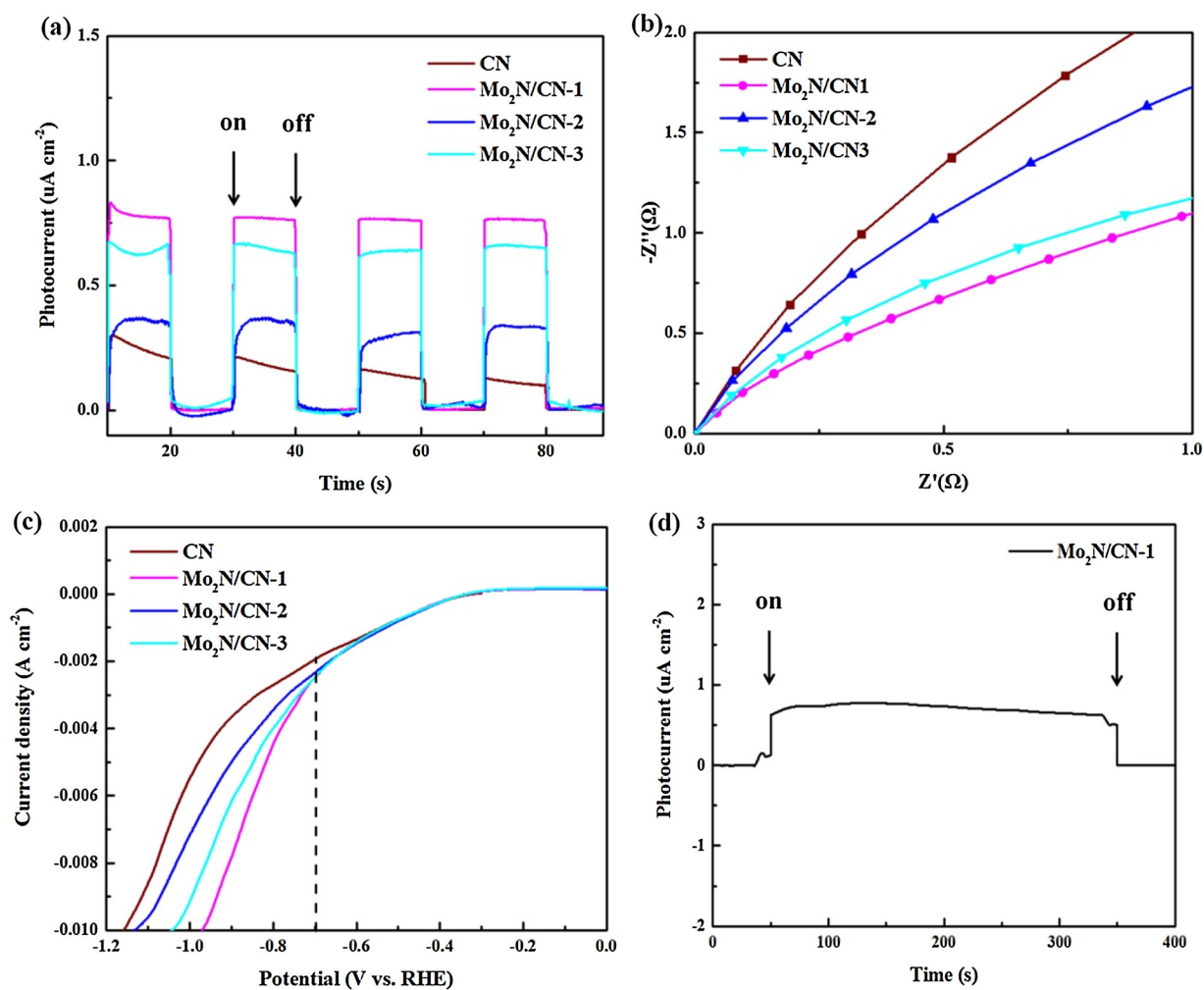
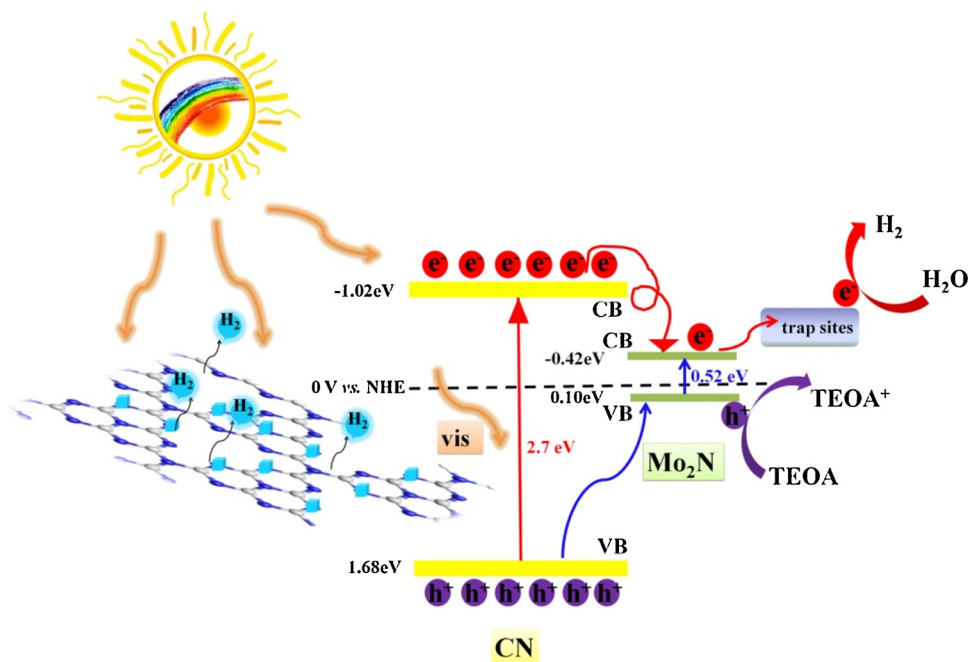


Fig. 8. Electrical properties: photocurrent response (a), EIS (b) and LSV (c) of CN and Mo₂N/CN-x, and photocurrent response under continuous irradiation of Mo₂N/CN-1(d).



Scheme 2. The mechanism of MoN/CN as a photocatalyst for water splitting.

absorption, charge transport, and mass transportation [41]. The Mo_2N shows the morphology of bulk originally. However after treating with 70°C oil bath in mixed solution with ethanol/water, the large-scale bulk Mo_2N can be converted to Mo_2N nanoparticles (Figs. S1b, 2a, and 3a), with the lateral size of 60 nm and the height of around 10 nm (shown in Fig. 2b–d). The AFM images (Fig. 2b–d) further show that Mo_2N nanoparticles show tightly fully heterojunctioned on the surface of CN, leading to the full effects of the cocatalysts to sacrifice more holes which may be one of the reasons for the increasing of H_2 generation.

To clarify the morphology of $\text{Mo}_2\text{N}/\text{CN}$ and the interfacial interaction between Mo_2N and CN in $\text{Mo}_2\text{N}/\text{CN}$, TEM images and corresponding EDX elemental mapping of Mo, N, and C elements have been investigated (Fig. 3). At first, the low-resolution TEM image show the typical morphology of a larger area of pieces of $\text{Mo}_2\text{N}/\text{CN}$ (Fig. 3a). The large pieces of CN nanosheets stacking layer by layer are not crystallized (Fig. 3b). And some Mo_2N nanoparticles have been loaded on the surface of CN correspondingly. To analyze the interface interaction of Mo_2N nanoparticles and CN, HRTEM images for the interface of two components have been shown in Fig. 3b. A clear lattice fringe with an interplanar distance of 0.24 nm from the HRTEM corresponds to the (111) crystal planes for Mo_2N nanoparticles which is related to the XRD pattern in Fig. 1a. Furthermore, Figs. 2c and 3b also display distinct interface interactions in the $\text{Mo}_2\text{N}/\text{CN}$ junctions, evidently expressing the formed heterojunction between Mo_2N nanoparticles and CN nanosheets. Also, combined Figs. 2c with 3b, it is easily concluded that the interface interaction may be caused by the two planes about Mo_2N (111) and CN (200), and the interaction between Mo_2N (111) planes and CN (002) planes at the interface in $\text{Mo}_2\text{N}/\text{CN}$ plays a crucial role to improve the catalytic performance. The STEM image of the $\text{MoN}/\text{g-C}_3\text{N}_4$ hybrids and corresponding EDX elemental mapping of Mo, N, and C elements evidently show the uniform hybridization of Mo_2N and CN (Fig. 3c–g). Furthermore, the electron diffraction image of $\text{Mo}_2\text{N}/\text{CN}$ is shown in Fig. 3h.

Furthermore, to investigate the existence of Mo_2N in the composite as well as the chemical configurations between Mo_2N and CN interfacial interactions, XPS spectra have been used to confirm C 1s, N 1s, Mo 3d and Mo 3p-N1s, as shown in Fig. 4. Distinct peaks in the overview survey spectrum (Fig. S2) show the existence of Mo, N and C elements. As shown in Fig. 4d, the peaks at 400.46 and 398.82 eV can correspond to Mo–O and Mo–N band, respectively, confirming the formation of Mo_2N . And the formation of Mo–O band may be caused by the exposure of the materials in air. Fig. 4c contains XPS spectra of the Mo 3d of the MoN/CN composite, in which the peaks can be fitted to three oxidation states (+3, +4, and +6) for element Mo. In the context of the analysis of bond distances, the peaks centered at higher binding energy (235.57/232.35 eV) are ascribed to Mo^{6+} due to surface Mo species that have been oxidized upon air exposure; the other pair of peaks at 232.94 and 229.77 eV are assigned to Mo^{4+} in the prismatic layer; and the last two peaks located at 231.70 and 228.66 eV are corresponded to Mo^{3+} revealing the Mo–N bonds in molybdenum nitride. As we know, Mo^{3+} is benefit for HER.

It is essential to understand N 1s XPS peaks for nitride compounds. For the N 1s spectrum of MoN/CN (Fig. 4b), there are three components at 400.87, 399.76, and 399.07 eV, corresponding to amino groups (C–N–H), tertiary nitrogen $\text{C}\equiv\text{N}$ groups and sp^2 bonded N (C–N=C) in the framework respectively. Also, the other two peaks at 397.67 and 395.01 eV are attributed to Mo_2N , confirming the strong interfacial interactions between Mo_2N and CN as well as investigating the formation of $\text{Mo}_2\text{N}/\text{CN}$ heterostructure. In addition, the C 1s peak of the $\text{Mo}_2\text{N}/\text{CN}$ heterostructure is also present. Two main peaks have been observed at the binding energies of 284.84 and 288.52 eV in C 1s spectrum displaying the existence of CN. (Fig. 4a) The binding energy at 284.84 is attributed to adventitious hydrocarbons. And the binding energy at 288.52 eV is assigned to N–C=N coordination. Therefore, the XPS results confirm that MoN have been hybridized with CN, which can be believed to enhance the catalytic activities by introducing more

charge carriers and improving the interaction of active sites with protons.

Since the photocatalytic activity of a photocatalyst usually depends on its optical absorption property, we analyze the optical properties of the structural variety of CN after hybridized with Mo_2N by UV–vis diffuse reflectance spectra (UV–vis DRS) as shown in Fig. 5a. In contrast, Mo_2N nanoparticles exhibit strong and broad photo-absorption in the wavelength range of 250–800 nm. CN displayed a clear visible absorption edge at around 424 nm. When Mo_2N was hybridized with CN, the edge of light absorption for $\text{Mo}_2\text{N}/\text{CN}$ can display a slight red-shift. The extended light absorption will be conducive to the high application of sunlight, benefitting for the values of photocatalysts. Based on the results of transformed Kubelka–Munk function $(\alpha h\nu)^2$ versus the energy exciting light $(h\nu)$ (shown in Fig. 5b), the bandgaps of CN, $\text{Mo}_2\text{N}/\text{CN}$ -1, $\text{Mo}_2\text{N}/\text{CN}$ -2, and $\text{Mo}_2\text{N}/\text{CN}$ -3 are estimated to be 2.70, 2.66, 2.78, and 2.54 eV, respectively. We can see that introducing Mo_2N can result in the narrower bandgap for $\text{Mo}_2\text{N}/\text{CN}$.

To further understand the photoinduced carrier separation mechanism, the Mott–Schottky (MS) plots of Mo_2N and CN have been obtained from the impedance potential tests to address the flat band potential and bandgap structure. As shown in Fig. 5d and e, the MS plots of CN and Mo_2N show the types of conductivity for them as well as their electronic conductivity. Both Mo_2N and CN belong to n-type semiconductor due to the positive slopes. Semiconductor theory holds that in the flat band state, the flat band potential is equal to the Fermi level. The flat band potentials for Mo_2N and CN are -0.22 and -0.82 V vs. RHE, respectively. Thus, it is confirmed that the conduction band (CB) potentials of Mo_2N and CN are -0.42 , and -1.02 eV vs. NHE, respectively. According to the bandgap (Fig. 5b), the valence band (VB) of Mo_2N and CN can be calculated to be 0.10, and 1.68 eV vs. NHE. Also, the MS plots of $\text{Mo}_2\text{N}/\text{CN}$ -1 have been measured at different frequencies as shown in Fig. 5f. Based on the electronic structure (Fig. 6), the transfer of the carriers can be illustrated clearly. When the light is irradiated on the surface of CN, the electrons on the CB of CN will transfer to the CB of Mo_2N . To some extent, it restrains the recombination of photo-generated carriers. In addition, Mo_2N as a kind of transition-metal nitrides promotes the transfer of carriers which has high conductivity and low electrical resistance. Thus, the hybridized band structure upgrades the transfer and curbs the recombination of electron–holes.

The photocatalytic activity of the samples has been further evaluated by H_2 generation from water in the presence of triethanolamine (TEOA) as sacrificed electron donors to quench holes from band-gap excitation. A trace amount of H_2 (about 0.1 μmol) can be detected when only CN is used as a kind of photocatalyst under visible light ($\lambda > 420$ nm) irradiation (Fig. 7a), suggesting the fast recombination of photogenerated carriers in pure CN. While the photocatalyst has change to the $\text{MoN}/\text{g-C}_3\text{N}_4$ composites, the amount of H_2 will increase apparently. As shown in Fig. 7a, the amount of H_2 can raise with increasing the irradiation time and reach 0.098, 13.35, 4.31, and 6.48 μmol after 3 h of visible light ($\lambda > 420$ nm) irradiation for CN, $\text{Mo}_2\text{N}/\text{CN}$ -1, $\text{Mo}_2\text{N}/\text{CN}$ -2, $\text{Mo}_2\text{N}/\text{CN}$ -3, respectively. The average H_2 production rate of $\text{Mo}_2\text{N}/\text{CN}$ -1 can be calculated to be 0.89 $\mu\text{mol g}^{-1} \text{h}^{-1}$, (Fig. 7b) which is 143 times higher than that of pure CN, indicating evidently that $\text{Mo}_2\text{N}/\text{CN}$ can serve as an efficient noble-metal free photocatalyst for H_2 evolution. The monochromatic incident photon-to-electron conversion efficiency (IPCE) has been estimated to be 1.75% at $\lambda = 400 \pm 15$ nm (Fig. 7d). In addition to high performance, the recycling performance and durability of photocatalysts are also important from the widespread practical applications. Four cycles of 3 h each with the samples have been conducted. As displayed in Fig. 7c, the H_2 production rate remains fairly constant (ca. 0.57 $\mu\text{mol g}^{-1} \text{h}^{-1}$) with no significant leveling off tendency for 12 h, revealing that the $\text{MoN}/\text{g-C}_3\text{N}_4$ heterojunctioned photocatalyst has excellent stability for long-term photocatalytic H_2 evolution. Additionally, the H_2 generation under full the spectrum light irradiation can reach 3.44

$\mu\text{mol g}^{-1} \text{h}^{-1}$ for $\text{Mo}_2\text{N}/\text{CN}-1$, which is higher than that of pure CN (Fig. S3).

The enhanced H_2 evolution may be caused by the fast charge transfer and carriers separation. The charge transfer, separation and recombination processes of photo-generated charge carriers in CN and $\text{Mo}_2\text{N}/\text{CN}$ have been studied by a set of photoelectron-chemical (PEC) experiments in a typical three-electrode system without any sacrificial agent. The transient photocurrent responses of CN and series of $\text{Mo}_2\text{N}/\text{CN}$ samples provide convincing evidence for the separation of photo-generated electron-hole pairs over several on-off photoirradiation ($\lambda > 420 \text{ nm}$) cycles. Fig. 8a shows that the photocurrent responses of all samples can reproducibly change under photoirradiation and recover quickly in the dark. Moreover, $\text{Mo}_2\text{N}/\text{CN}$ exhibits much higher transient photocurrent than pure CN samples, indicating the higher electron-hole pairs separation efficiency in the heterostructures because of the existence of Mo_2N . And the highest photocurrent is from $\text{Mo}_2\text{N}/\text{CN}-1$. Meanwhile, the better stability of $\text{Mo}_2\text{N}/\text{CN}-1$ is tested again by the continuous photocurrent for 300 s which is shown in Fig. 8d. Besides the measurements of photocurrent, the electrochemical impedance spectroscopy (EIS) is used to gain a better understanding of the HER kinetics occurring at the electrode/electrolyte interface to support for the separation of electron-hole pairs. As shown in Fig. 8b, the Nyquist plots of all $\text{Mo}_2\text{N}/\text{CN}$ samples exhibit decreased arc radii compared to that of pure CN, suggesting that the synergies effect of Mo_2N and CN induces smaller interface resistance between Mo_2N and CN, and consequently facilitates charge transport and transfer. Then, the sample of $\text{Mo}_2\text{N}/\text{CN}-1$ shows the smallest arc radius with displaying the lowest charge transfer resistance. In addition, linear sweep voltammetry (LSV) curves (Fig. 8c) obtained from CN and $\text{Mo}_2\text{N}/\text{CN}$ show that only a quite low photocurrent can be observed for individual CN throughout the whole potential range under light irradiation. In contrast, all the $\text{Mo}_2\text{N}/\text{CN}$ samples exhibit reduced onset overpotentials, indicating that the forming heterostructures between Mo_2N and CN improve the catalytic activity. At the same time, the photocurrent density obtained on the $\text{Mo}_2\text{N}/\text{CN}-1$ electrode reaches 7 mA cm^{-2} under the bias of -0.9 V which is about 2.3 folds of that of pure CN electrode. The catalysts display significantly enhanced photocurrent density after the formation of heterostructures, reflecting that coupling Mo_2N and CN could facilitate the charges separation and migration. The consistent result is also supported by transient photocurrent measurements as illustrated in Fig. 8a.

The PL spectra in Fig. 5c are employed to accurately investigate the migration, transfer, and recombination process of the photo-generated charge carriers together with the role of Mo_2N nanoparticles during the photocatalytic process [42]. In general, the intensity of PL emission peak is an intrinsic characteristic of the recombination of charge carriers for materials. As shown in Fig. 5c, a strong PL emission peak at about 450 nm from $\text{g-C}_3\text{N}_4$ can be attributed to the band-band PL phenomenon of the photoinduced charge carriers. In comparison to pure CN samples, the emission peaks intensity of $\text{Mo}_2\text{N}/\text{CN}$ heterostructure is much weaker than that of pure CN samples. This phenomenon indicated that the recombination is retarded and the efficient separation of charge carriers is accelerated at the interface of Mo_2N and CN, thus introducing much more free electrons to participate in the photocatalytic reactions. Also, the sample of $\text{Mo}_2\text{N}/\text{CN}-1$ shows the weakest peak intensity, indicating the lowest recombination of photo-induced carriers which resonates with the PEC spectra (Fig. 7) and the H_2 evolution characters (Fig. 6).

As we all know, it is crucial to have an efficient charge transfer/separation for the enhancement of the photocatalytic performance. According to the photocatalytic experiments, the high H_2 evolution performance and efficient charge transfer and separation may be caused by the bandgap of the samples which is concluded that the VB and CB of CN and Mo_2N are 1.68 , -1.02 eV and 0.10 , -0.42 eV , respectively. From the point of band structure of Mo_2N and CN, a type I heterojunction is expected at their interface when Mo_2N is attached on the

surface of CN shown in Scheme 2. Mo_2N possesses a lower CB and a higher VB than pure CN. When $\text{Mo}_2\text{N}/\text{CN}$ is irradiated with visible light ($\lambda > 420 \text{ nm}$), the CN is excited to generate electrons and holes. Mo_2N acts as an electron acceptor from adjacent CN, reducing the recombination of photogenerated charges in CN. The PL spectra also verifies the recombination of carriers in $\text{Mo}_2\text{N}/\text{CN}$ is much lower than that in CN (Fig. 5d). The electrons generated from the CB of CN quickly transfer to the CB of Mo_2N reduction active sites to participate in the H_2 evolution. Meanwhile, the holes on the VB of CN react with TEOA. In addition, some of the holes from the VB of CN can transfer to the VB of Mo_2N . The photocatalytic H_2 evolution which reflects the function of the separation of photogenerated carriers of $\text{Mo}_2\text{N}/\text{CN}$ matches well with the results of PL, photocurrent, LSV, and EIS. All data show that the electron transfer pathway on $\text{Mo}_2\text{N}/\text{CN}$ improves the separation rate of photogenerated electron-hole pairs which can greatly enhance the photocatalytic activity.

4. Conclusions

In conclusion, $\text{Mo}_2\text{N}/\text{CN}$ was constructed via oil bathing method and Mo_2N was used to form heterostructure with $\text{g-C}_3\text{N}_4$ for enhancing the property of $\text{g-C}_3\text{N}_4$ in photocatalytic hydrogen evolution for the first time. Besides, 2D $\text{g-C}_3\text{N}_4$ ultrathin nanosheets were successfully obtained via adjusting the pH of urea/water solution by dropping into HCl solution. In the presence of TEOA as a sacrificial agent, without any noble metal, H_2 evolution can be greatly enhanced (about 143 times) under visible light irradiation compared with CN, and it reached up to $0.89 \mu\text{mol g}^{-1} \text{h}^{-1}$. First, Mo^{3+} from the Mo_2N samples is beneficial for HER activities. Then, Mo_2N acts as electron acceptor for the excited CN, resulting in the barrier of recombination for carriers. Meanwhile, the 2D ultrathin layer morphology of CN makes the electron moving path narrow, high charge transfer rate and more active sites exposure. In particular, the interaction between Mo_2N (111) planes and $\text{g-C}_3\text{N}_4$ (002) planes at the interface in $\text{Mo}_2\text{N}/\text{CN}$ plays a crucial role in the improved catalytic performance. The unique growing direction of Mo_2N can be benefit for full integration between Mo_2N and CN to produce more active surface area. The present results show the advantages of $\text{Mo}_2\text{N}/\text{CN}$ as a non-noble photocatalyst with high H_2 generation in the visible region, and open a new avenue about transition metal nitride in photocatalytic water splitting in developing a new energy conversion system.

Acknowledgements

This work was supported by the National Natural Science Foundation of China (NSFC) (Grants Nos. 21671133; 21271010, 21604051, 21507081); the Shanghai Municipal Education Commission (Nos. 15ZZ088; 15SG49); Technology Commission of Shanghai Municipality (18020500800) and International Joint Laboratory on Resource Chemistry.

Appendix A. Supplementary data

Supplementary material related to this article can be found, in the online version, at doi:<https://doi.org/10.1016/j.apcatb.2018.07.040>.

References

- [1] M.S. Dresselhaus, I.L. Thomas, Alternative energy technologies, *Nature* 414 (2001) 332–337.
- [2] Z.W. She, J. Kibsgaard, C.F. Dickens, I. Chorkendorff, J.K. Nørskov, T.F. Jaramillo, Combining theory and experiment in electrocatalysis: insights into materials design, *Science* 355 (2017) ead4998.
- [3] L. Lin, W. Zhou, R. Gao, S. Yao, X. Zhang, W. Xu, S. Zheng, Z. Jiang, Q. Yu, Y.W. Li, C. Shi, X.D. Wen, D. Ma, Low-temperature hydrogen production from water and methanol using Pt/ α -MoC catalysts, *Nature* 544 (2017) 80–83.
- [4] M.G. Walter, E.L. Warren, J.R. McKone, S.W. Boettcher, Q. Mi, E.A. Santori, N.S. Lewis, Solar water splitting cells, *Chem. Rev.* 110 (2010) 6446.

- [5] X.X. Zou, Y. Zhang, Noble metal-free hydrogen evolution catalysts for water splitting, *Chem. Soc. Rev.* 44 (2015) 5148–5180.
- [6] G.G. Zhang, Z.A. Lan, X.C. Wang, Conjugated polymers: catalysts for photocatalytic hydrogen evolution, *Angew. Chem. Int. Ed.* 55 (2016) 15712–15727.
- [7] K. Zhang, J.K. Kim, B. Park, S. Qian, X. Sheng, H. Zeng, H. Shin, S.H. Oh, C.L. Lee, J.H. Park, Defect induced epitaxial growth for efficient solar hydrogen production, *Nano Lett.* 17 (2017) 6676–6683.
- [8] Y. Qi, S.S. Chen, M.R. Li, Q. Ding, Z. Li, J.Y. Cui, B.B. Dong, F.X. Zhang, C. Li, Achievement of visible-light-driven Z-scheme overall water splitting using barium-modified Ta_3N_5 as an H_2 -evolving photocatalyst, *Chem. Sci.* 8 (2017) 437–443.
- [9] F.Q. Zhou, J.C. Fan, Q.J. Xu, Y.L. Min, BiVO_4 nanowires decorated with CdS nanoparticles as Z-scheme photocatalyst with enhanced H_2 generation, *Appl. Catal. B* 201 (2017) 77–83.
- [10] J. Hu, Z. Guo, P.E. McWilliams, J.E. Darges, D.L. Druffel, A.M. Moran, S.C. Warren, Band gap engineering in a 2D material for solar-to-chemical energy conversion, *Nano Lett.* 16 (2016) 74–79.
- [11] H. Kato, K. Asakura, A. Kudo, Highly efficient water splitting into H_2 and O_2 over lanthanum-doped NaTaO_3 photocatalysts with High crystallinity and surface nanostructure, *J. Am. Chem. Soc.* 125 (2003) 3082.
- [12] P.V. Kamat, J.A. Christians, Solar cells versus solar fuels: two different outcomes, *J. Phys. Chem. Lett.* 6 (2015) 1917.
- [13] X.C. Wang, K. Maeda, A. Thomas, K. Takanabe, G. Xin, J.M. Carlsson, K. Domen, M. Antonietti, A metal-free polymeric photocatalyst for hydrogen production from water under visible light, *Nat. Mater.* 8 (2009) 76.
- [14] Y. Wang, J. Zhang, X. Wang, M. Antonietti, H. Li, Boron-and fluorine-containing mesoporous carbon nitride polymers: metal-free catalysts for cyclohexane oxidation, *Angew. Chem. Int. Ed.* 49 (2010) 3356.
- [15] J. Liu, Y. Liu, N. Liu, Y. Han, X. Zhang, H. Huang, Y. Lifshitz, S.T. Lee, J. Zhang, Z. Kang, Metal-free efficient photocatalyst for stable visible water splitting via a two-electron pathway, *Science* 347 (2015) 970.
- [16] X. Wang, X. Chen, A. Thomas, X. Fu, M. Antonietti, Metal-Containing carbon nitride compounds: a new functional organic–metal hybrid material, *Adv. Mater.* 21 (2009) 1609.
- [17] Q. Han, B. Wang, J. Gao, Z.H. Cheng, Y. Zhao, Z.P. Zhang, L.T. Qu, Atomically thin mesoporous nanomesh of graphitic C_3N_4 for high-efficiency photocatalytic hydrogen evolution, *ACS Nano* 10 (2016) 2745.
- [18] Q.H. Liang, Z. Li, X.L. Yu, Z.H. Huang, F.Y. Kang, Q.H. Yang, Macroscopic 3D porous graphitic carbon nitride monolith for enhanced photocatalytic hydrogen evolution, *Adv. Mater.* 27 (2015) 4634.
- [19] S.E. Guo, Z.P. Deng, M.X. Li, B.J. Jiang, C.G. Tian, Q.J. Pan, H.G. Fu, Phosphorus-doped carbon nitride tubes with a layered micro-nanostructure for enhanced visible-light photocatalytic hydrogen evolution, *Angew. Chem. Int. Ed.* 55 (2016) 1830.
- [20] G. Dong, K. Zhao, L. Zhang, Carbon self-doping induced high electronic conductivity and photoreactivity of g- C_3N_4 , *Chem. Commun.* 48 (2012) 6178.
- [21] J.S. Zhang, J.H. Sun, K. Maeda, K. Domen, P. Liu, M. Antonietti, X.Z. Fu, X.C. Wang, Sulfur-mediated synthesis of carbon nitride: band-gap engineering and improved functions for photocatalysis, *Energy Environ. Sci.* 4 (2011) 675.
- [22] Y. Li, Z. Wang, T. Xia, H. Ju, K. Zhang, et al., Implementing metal-to-ligand charge transfer in organic semiconductor for improved visible-near-infrared photocatalysis, *Adv. Mater.* 28 (2016) 6959.
- [23] D. Mongin, E. Shaviv, P. Maioli, A. Crut, U. Banin, N. Del Fatti, F. Vallee, Ultrafast photoinduced charge separation in metal-semiconductor nanohybrids, *ACS Nano* 6 (2012) 7034–7043.
- [24] A.B. Laursen, S. Kegnæs, S. Dahl, I. Chorkendorff, Molybdenum sulfides-efficient and viable materials for electro-and photoelectrocatalytic hydrogen evolution, *Energy Environ. Sci.* 5 (2012) 5577–5591.
- [25] K. Chang, Z. Mei, T. Wang, Q. Kang, S. Ouyang, J. Ye, MoS_2 /Graphene cocatalyst for efficient photocatalytic H_2 evolution under visible light irradiation, *ACS Nano* 8 (2014) 7078–7087.
- [26] X. Zong, H. Yan, G. Wu, G. Ma, F. Wen, L. Wang, C. Li, Enhancement of photocatalytic H_2 evolution on CdS by loading MoS_2 as cocatalyst under visible light irradiation, *J. Am. Chem. Soc.* 130 (2008) 7176–7177.
- [27] Y. Zhang, B. Ouyang, J. Xu, S. Chen, R.S. Rawat, H.J. Fan, 3D porous hierarchical Nickel–Molybdenum nitrides synthesized by RF plasma as highly active and stable hydrogen-evolution-reaction electrocatalysts, *Adv. Energy Mater.* 6 (2016) 201600221.
- [28] X.Z. Yue, S.S. Yi, R.W. Wang, Z.T. Zhang, S.L. Qiu, A novel architecture of dandelion-like $\text{Mo}_2\text{C}/\text{TiO}_2$ heterojunction photocatalysts towards high-performance photocatalytic hydrogen production from water splitting, *J. Mater. Chem. A* 5 (2017) 10591.
- [29] Y. Jin, H. Wang, J. Li, X. Yue, Y. Han, P.K. Shen, Y. Cui, Porous MoO_3 nanosheets as non-noble bifunctional electrocatalysts for overall water splitting, *Adv. Mater.* 28 (2016) 3785–3790.
- [30] Z.C. Zhuang, Y. Li, Z.L. Li, F. Lv, Z.Q. Lang, K.N. Zhao, L. Zhou, L. Moskaleva, S.J. Guo, L.Q. Mai, Schottky catalysts boost hydrogen evolution: the case of $\text{MoB}/\text{g-C}_3\text{N}_4$ interface materials, *Angew. Chem. Int. Ed.* 57 (2017).
- [31] J.G. Chen, Carbide and nitride overlayers on early transition metal surfaces: preparation, characterization, and reactivities, *Chem. Rev.* 96 (1996) 1477.
- [32] D.J. Ham, J.S. Lee, Transition metal carbides and nitrides as electrode materials for low temperature fuel cells, *Energies* 2 (2009) 873.
- [33] W.F. Chen, K. Sasaki, C. Ma, A.I. Frenkel, N. Marinovic, J.T. Muckerman, Y. Zhu, R.R. Adzic, Hydrogen-evolution catalysts based on non-noble metal nickel–molybdenum nitride nanosheets, *Angew. Chem. Int. Ed.* 51 (2012) 6131.
- [34] Jf. Xie, S. Li, X.D. Zhang, J.J. Zhang, R.X. Wang, H. Zhang, B.C. Pan, Y. Xie, Atomically-thin molybdenum nitride nanosheets with exposed active surface sites for efficient hydrogen evolution, *Chem. Sci.* 5 (2014) 4615.
- [35] C.L. Tan, X.H. Cao, X.J. Wu, Q.Y. He, J. Yang, X. Zhang, J.Z. Chen, W. Zhao, S.K. Han, G.H. Nam, M. Sindoro, H. Zhan, Recent advances in ultrathin two-dimensional nanomaterials, *Chem. Rev.* 117 (2017) 6225–6331.
- [36] H. Yu, L. Shang, T. Bian, R. Shi, G.I. Waterhouse, Y. Zhao, C. Zhou, L.Z. Wu, C.H. Tung, T. Zhang, Nitrogen-doped porous carbon nanosheets templated from g- C_3N_4 as metal-free electrocatalysts for efficient oxygen reduction reaction, *Adv. Mater.* 28 (2016) 5080–5086.
- [37] Z. Zhang, K. Liu, Z. Feng, Y. Bao, B. Dong, Hierarchical sheet-on-sheet $\text{ZnIn}_2\text{S}_4/\text{g-C}_3\text{N}_4$ heterostructure with highly efficient photocatalytic H_2 production based on photoinduced interfacial charge transfer, *Sci. Rep.* 6 (2016) 19221.
- [38] Y.P. Zhu, T.Z. Ren, Z.Y. Yuan, Mesoporous phosphorus-doped g- C_3N_4 nanostructured flowers with superior photocatalytic hydrogen evolution performance, *ACS Appl. Mater. Interfaces* 7 (2015) 16850–16856.
- [39] Q. Han, B. Wang, Y. Zhao, C.G. Hu, L.T. Qu, A graphitic- C_3N_4 “Seaweed” architecture for enhanced hydrogen evolution, *Angew. Chem. Int. Ed.* 54 (2015) 11433.
- [40] Q.Y. Lin, L. Li, S.J. Liang, M.H. Liu, J.H. Bi, L. Wu, Efficient synthesis of monolayer carbon nitride 2D nanosheet with tunable concentration and enhanced visible-light photocatalytic activities, *Appl. Catal. B* 163 (2015) 135.
- [41] T.R. Chetia, M.S. Ansari, M. Qureshi, Graphitic carbon nitride as a photovoltaic booster in quantum dot sensitized solar cells: a synergistic approach for enhanced charge separation and injection, *J. Mater. Chem. A* 4 (2016) 5528–5541.
- [42] J. Zhang, L. Qi, J. Ran, J. Yu, S.Z. Qiao, Ternary $\text{NiS}/\text{ZnxCd1-xS}$ /reduced graphene oxide nanocomposites for enhanced solar photocatalytic H_2 -production activity, *Adv. Energy Mater.* 4 (2014) 1301925–1301930.